

Received July 8, 2019, accepted August 1, 2019, date of publication August 7, 2019, date of current version September 3, 2019.

Digital Object Identifier 10.1109/ACCESS.2019.2933775

# Deterministic Modeling of 5G Millimeter-Wave Communication in an Underground Mine Tunnel

MOHAMAD GHADDAR<sup>1</sup>, ISMAIL BEN MABROUK<sup>1,2</sup>,  
MOURAD NEDIL<sup>1</sup>, (Senior Member, IEEE), KHELIFA HETTAK<sup>3</sup>,  
AND LARBI TALBI<sup>4</sup>, (Senior Member, IEEE)

<sup>1</sup>Underground Communications Laboratory, University of Quebec in Abitibi-Temiscamigue (UQAT), Val-d'Or, QC J9P 1Y3, Canada

<sup>2</sup>Networks and Communication Engineering Department, Al Ain University of Science and Technology, Abu Dhabi 64141, UAE

<sup>3</sup>Communications Research Centre, Ottawa (CRC), ON K2H 8S2, Canada

<sup>4</sup>Computer Sciences and Engineering Department, University of Quebec in Outaouais, Gatineau, QC J8X 3X7, Canada

Corresponding author: Ismail Ben Mabrouk (ismail.mabrouk@aau.ac.ae)

This work was supported in part by the Natural Sciences and Engineering Research Council of Canada (NSERC).

**ABSTRACT** This paper presents broadband simulations and measurements of Millimeter-Waves (mm-wave) propagation in a rugged underground mine environment. Mathematical formulation was carried out in the framework of Uniform Theory of Diffraction (UTD) to develop a deterministic Ray-Tracing (RT) model under Line-Of-Sight (LOS) condition. The developed theoretical model was then validated experimentally in Frequency Domain (FD) and Time Domain (TD). A significant agreement between simulations and measurements is achieved in both domains. The rough surfaces of the mine are modeled deterministically as groups of diffracting wedges having random dimensions (heights, angles) being transversely oriented throughout the gallery. Acute (inferior to 30°) and obtuse (superior to 120°) wedges angles are found to have significant effects on the overall propagation performance. In the mm-wave band, the UTD diffraction phenomenon is evident and must be considered in the design of underground mine channels. In fact, the presented model is found to be capable of predicting the complex multipath of underground mine channels, due to the ray-optical behavior at mm-wave bands.

**INDEX TERMS** Power delay profile, ray tracing, radio propagation, underground mining.

## I. INTRODUCTION

Thanks to the recent development of the 5G and IoT technologies, the underground mining industry is expected to evolve into a new era of “smart mining mobility” where infrastructures, mining machinery, and miners will be interconnected to achieve optimal automation, mobility, ultra-high safety, and productivity. Future underground mining environment will require various high data rates applications such as video surveillance, onsite real-time high-data rate connectivity for mining operation information and relay video transmissions for monitoring and safety purposes. This advanced technology is favorable for multi-Gb/s applications and has attracted significant attention with its promise toward the operation of mm-wave communications within underground mine galleries. Previous research studies in tunnel environments including highway, railway and underground mine were limited to the low-frequency bands [1]–[4]. In fact, microwave

bands suffer from narrow bandwidth and have been widely investigated [5], [6]. Moreover, relevant literature review about wall surface roughness effect on propagation channel in tunnels is scarce. This effect is a source of an important path loss, and therefore should be taken into consideration for a rigorous prediction of the signal power. Although, the long history of channel propagation within tunnels, the impact of roughness on tunnel propagation is barely analyzed. Published results in the literature provide “rules of thumb” and guidelines to understand the impact of various environmental characteristics. Back in 1974, Mahmoud et al [7] studied the effect of roughness on the signal attenuation in a parallel-plate waveguide. Later, the first model for analyzing the roughness effect in a rectangular tunnel is developed by Emslie *et al.* [8]. Martelly et al. [9] estimated theoretically the roughness effect applying the vector parabolic equation approach, and proved it is consistent with Emslie's model presented in [8]. Latest studies based on experimental mm-wave channel measurements were performed in an underground mine and subway tunnels [10], [11]. The roughness of the

The associate editor coordinating the review of this article and approving it for publication was Chong Han.

tunnel walls is identified as the origin of reducing the delay spread and the removal of the waveguide effect in a tunnel. Moreover, it has been shown that the channel path loss depends more on the tunnel size than the tunnel geometry and shape [12]. In [13], a theoretical channel modeling in tunnels is presented under complex meteorological scenarios, such as fog, sand, and wind. The modeling is based on the parabolic equation method. After, calculating the meteorological environment effective permittivity, the propagation channel is modeled by updating the refractive index. In [14], a measurement campaign and ray tracing simulations are carried out within a subway tunnel at the mm-wave frequency band. Good agreement between measurements and simulations is observed. Results recommend the use of MIMO technology as a remarkable scheme for improving the performance of mm-wave communication in a tunnel environment. Authors in [15], examine the channel propagation at the mm-wave frequency band in a short tunnel using a time-domain channel measurement. Channel parameters, such as K-factor, root-mean-square delay spread, and shadowing are investigated. In [16] the study considers the channel performance of mm-wave MIMO system in a subway tunnel, using ray-tracing-based simulations and experimental measurements. MIMO channel capacity is calculated for different scenarios. A high-gain directional horn antenna is recommended in [6] for MIMO channel measurements conducted in underground mine tunnels in order to overcome high propagation losses at 60-GHz frequency band. In fact, deterministic models can be considered as a viable approach to obtain channel parameters for a propagation environment in order to facilitate satisfactory interpretations of experimental results. Furthermore, absence of reliable ray-tracing (RT) simulators and models for mm-wave propagation in confined environment [17]–[20] are quite noteworthy. For indoor environments the shapes and the electrical properties of the surrounding surfaces are well determined. The propagation mechanism can be modeled as a free-space LOS superimposed by specular reflections from surrounding smooth surfaces. In contrast, randomly structured underground mines consist of corrugated surfaces with a high degree of roughness that renders the deterministic modeling of such channels very challenging.

The purpose of this study is twofold, firstly is to understand the propagation of mm-wave in the underground mine environment and its impact on the design, test and simulation of wireless systems. The second objective of this paper is the development of a global RT simulator for the extraction of channel parameters in the underground mine environment. The measurements are performed using a frequency-sweep technique to ensure real-time static characterization of the channel (stationary) free from the disturbances caused by moving objects. The rest of the paper is organized as follows. Section 2 describes the site location along with the measurement system and procedure. The mine gallery geological structure and mathematical modeling concept are presented in section 3 and the subsequent section 4 elaborates the simulation algorithm. An ideal channel analysis is provided

in section 5 and the experimental validation of the tracer is presented in section 6. Concluding remarks are then provided in section 7.

## II. MEASUREMENT HARDWARE SETUP, PROCEDURE AND SITE DESCRIPTION

The amplitude and phase variations of 21,600 complex tones across IEEE802.15.3c channel-1 (61.56–63.72 GHz) were measured using transmit power of 10dBm. Vertically polarized pyramidal horn antennas were used at both Tx and Rx antennas with the radiation gain of 23.4 dBi and 3-dB beam-width of 25°. Gain variation of the antennas quoted from manufacturer information sheets is shown in Fig. 1 which amounts to a slight variation of 0.25 dB (23.2–23.45 dB) across the band of interest. The gain variation can be calibrated out in the anechoic chamber for 1 m reference separation between  $T_X$  and  $R_X$ . A detailed description of the measurement system and the antenna configuration are presented in [6].

The site (4.2 m × 4.8 m × 70 m) is 70 m below the ground level in a mine that is operated by the Canadian Center for Minerals and Energy Technology (CANMET). The floor of the mine is rather flat and mostly covered by wet soil and water while the other three surrounding surfaces (i.e., two side walls and ceiling) are granite as shown in Fig. 1. During measurements, both  $T_X$  and  $R_X$  antennas were maintained at a height of 1.5 m on the central line of the gallery in order to capture efficiently the effect of all surrounding surfaces. To establish a LOS channel, the antennas were aligned by means of a laser alignment system and linear tracking vertex table. Averaging ( $N_s$ ) frequency sweeps (seven in this case), as described in [6], was used for each Rx position on the  $4 \times 4$  ( $N_x \times N_y$ ) points vertex table in order to mitigate the impact of random noise on measurements. The measured Channel Transfer Function (CTF) is then expressed as:

$$CTF_{meas.} = \frac{1}{N_s N_x N_y} \left\{ \sum_{i=1}^{N_s N_x N_y} \alpha(x, y, s, f) e^{j\theta(x, y, s, f)} \right\} \quad (1)$$

where  $\alpha(x, y, s, f)$  and  $\theta(x, y, s, f)$  are magnitude and phase of each frequency component  $f$ , respectively. “ $x, y$ ” are the coordinates on the vertex table and “ $s$ ” is the  $T_X$ – $R_X$  distance. The impact of the sounder’s hardware including the feeding cables and the antennas were calibrated out by normalizing all measured complex CTFs with respect to  $T_X$ – $R_X$  distance reference of 1 m [21].

$$CTF_{calibrated} = \frac{CTF_{meas.}}{CTF_{at 1m}} \quad (2)$$

Raw datas along with calibrated CTFs measured for 2 m separation between  $T_X$ – $R_X$  are shown in Fig. 2(a) and Fig. 2(b), respectively. Directional nature of Tx and Rx antennas mitigates multipaths and imposes similar gain and linear phase response across the band. Practically, the multipath effects are more pronounced at larger  $T_X$ – $R_X$  ranges, as it will be shown later at 10 m.

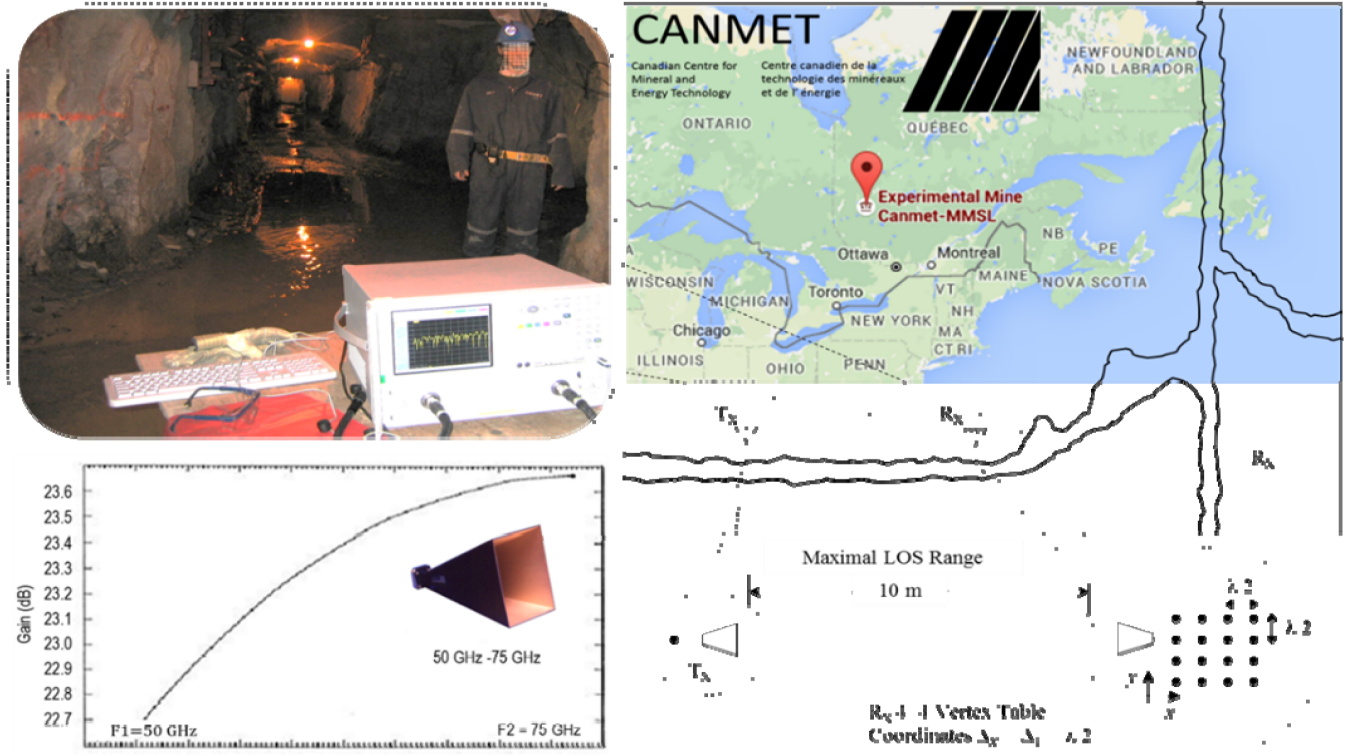


FIGURE 1. An illustrative map of CANMET underground mine gallery,  $T_x$ - $R_x$  locations, and Tx-Rx antenna performance.

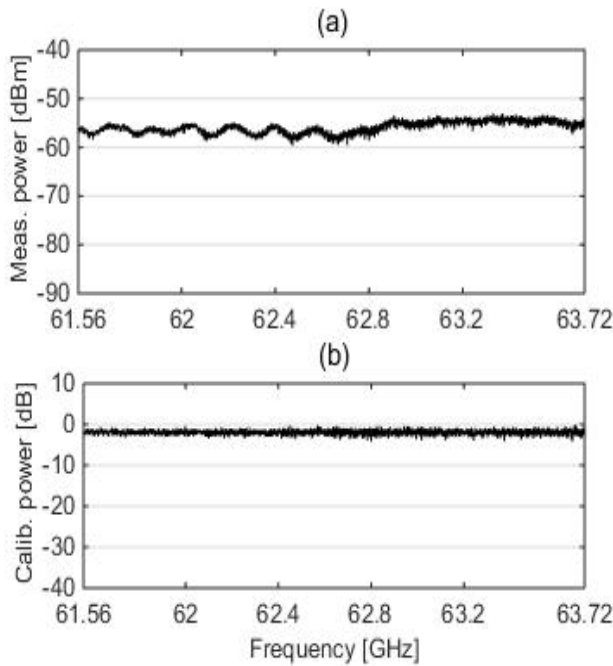


FIGURE 2. a) Measured and, b) Calibrated CTFs obtained at 2m of  $T_x$ - $R_x$  distance.

### III. SITE STRUCTURE AND MODELING CONCEPT

Random excavation operations in the gallery result in corrugated extremely rough surfaces. The depth of these randomly-curved surfaces varies at an average rate of 0.8 m

while their roughness is around 0.3 m, as illustrated in Fig.1. A signal with a wavelength shorter than the geometrical features of the surface of the gallery sees this corrugated rough surface as an aggregate of diffracting wedges with random angles and heights. Subsequent to a detailed investigation of the geological structure of the site, it was found that these edges tend to be oriented in the transverse direction with respect to the central line of the gallery (or LOS) as depicted in a Fig.1.

Uniform theory of diffraction (UTD) for the two dimensional (2D) wedge diffraction is illustrated in Fig. 3. The incidence angle ( $\phi'$ ) and diffraction angle ( $\phi$ ) are measured from  $0$ -face. The exterior angle of the wedge is denoted by  $n\pi$  and  $0 \leq n \leq 2$ . The incidence shadow boundary (ISB) and reflection shadow boundary (RSB) delineate the regions of space pertained to incident, reflected or diffracted rays. Hence, ISB and RSB are located at  $\phi_{ISB} = \pi + \phi'$  and  $\phi_{RSB} = \pi - \phi'$ , respectively. The UTD diffracted field is expressed as [22]:

$$E_{\perp, \parallel}(s) = E_i(s') D_{\perp, \parallel}(L, \phi, \phi') A(s', s) e^{-jks} \quad (3)$$

“ $\perp$ ” and “ $\parallel$ ” stand for soft and hard cases, in which the incident field ( $E_i$ ) is perpendicular and parallel to the plane of incidence, respectively.  $s$  and  $s'$  denote the path lengths of the incident and diffracted rays, respectively. The general equation of the incident field on the wedge is

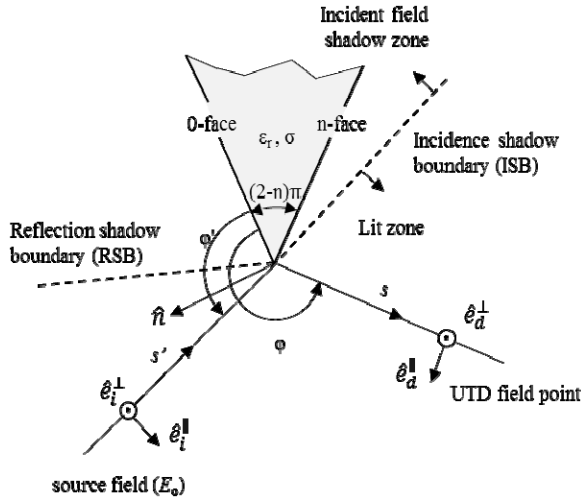


FIGURE 3. Uniform geometrical theory of diffraction (UTD) from a wedge.

expressed as:

$$E_i(s') = \frac{E_o e^{-jks'}}{s'} \quad (4)$$

$E_o$  is the relative amplitude of the spherical-wave source, its magnitude is assumed to be 1. The spreading factor  $A(s', s)$  is given as [22]:

$$A(s', s) = \sqrt{\frac{s'}{s(s' + s)}} \quad (5)$$

The heuristic UTD coefficient is expressed as [22], [23]:

$$D_{\parallel, \perp} = \frac{-e^{-j\pi/4}}{2n\sqrt{2\pi k s \sin(\gamma)}} \times \left\{ \cot\left(\frac{\pi + (\phi - \phi')}{2n}\right) F[kLa^+(\phi - \phi')] + \cot\left(\frac{\pi + (\phi - \phi')}{2n}\right) F[kLa^-(\phi + \phi')] + R_{\parallel, \perp}^0 \cot\left(\frac{\pi - (\phi + \phi')}{2n}\right) F[kLa^+(\phi - \phi')] + R_{\parallel, \perp}^n \cot\left(\frac{\pi - (\phi + \phi')}{2n}\right) F[kLa^-(\phi + \phi')] \right\} \quad (6)$$

$$L = \frac{ss'}{s + s'} \sin^2(\gamma) \quad (7)$$

$$a^\pm(\rho) = 2\cos^2\left(\frac{2n\pi N^\mp - \rho}{2}\right) \quad (8)$$

$$\rho = \phi \pm \phi' \quad (9)$$

$$2\pi n N^\pm - \rho = \pm\pi \quad (10)$$

“ $\gamma$ ” delineates the angle between the incident ray and the edge associated with the 3<sup>rd</sup> dimension of diffraction which is  $\gamma = \pi/2$ .  $R_{\parallel, \perp}^0$  and  $R_{\parallel, \perp}^n$  are Fresnel reflection coefficients corresponding to parallel and perpendicular polarizations, respectively, as defined for the illuminated wedge face (0-face) and the diffraction face (n-face). Such coefficients are dependent on the dielectric constants of reflecting surfaces. The Fresnel integral function which corrects the singularities at the shadow boundaries is defined as:

$$F(x) = 2j\sqrt{x}e^{ix} \int_{\sqrt{x}}^{\infty} e^{-j\tau^2} d\tau \quad (11)$$

In the mm-waves band, the relative dielectric constant and the conductivity of marble are ( $\epsilon_r = 11.56$ ) and ( $\sigma = 0.258\text{S/m}$ ), respectively [24]. The frequency-dependent complex dielectric constant is given as [25]:

$$\epsilon_r^* = \epsilon_r - j60\sigma\lambda \quad (12)$$

where  $\lambda$  is the operating wavelength.

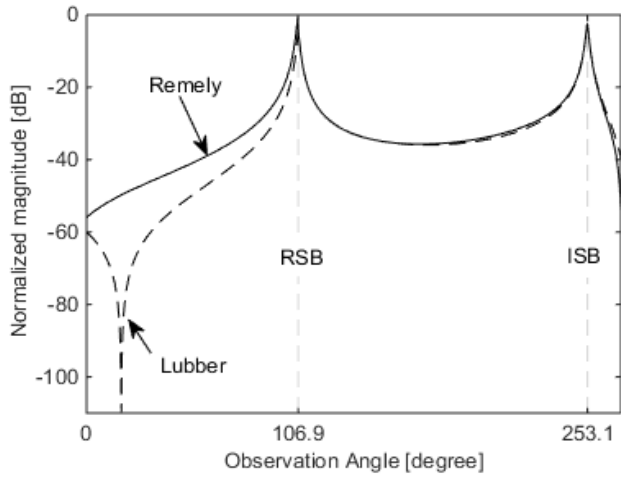
Noting the impact of the heuristic diffraction coefficients on the accuracy of results, simulations were performed to assess UTD for a diffracting edge. The expressions in [23] and [25] are efficient for the calculation of diffraction from a wide variety of wedges as they account for the dielectric constant of loss tangent of the wedges. Fig. 4(a) shows the plot of normalized diffracted field intensity with respect to  $R_X$  angular position ( $\phi$ ) while observation points are located on a circle of a radius ( $s = 5.5\text{ m}$ ) centered on a right angle ( $\beta = 90^\circ$ ) marble edge.

As observed, Lubber’s diffraction coefficient in [23] results in discontinuities away from ISB and RSB. In contrast, Remley’s expression in [25] shows a smooth and monotonic decrease in the diffracted field and provides a good approximation when  $R_X$  is in the deep shadow region. In this work, Remley’s method was observed to agree with the measured data resulted from single diffractions. Further simulations were then performed and the results are shown in Fig. 4(b) to investigate the effect of the wedges angles ( $\beta$ ) on the diffracted field. As observed, a change in the wedge angle from about  $79^\circ$  to  $1^\circ$  (or knife-edges) can lead to a diffraction boosting excess of 40 dB. The impact of the operating frequency is shown in Fig. 4(c) where computation at 900 MHz with the same parameters as in [25] resulted in a very good agreement. Therefore, 60 GHz link experiences an additional diffraction loss of about 20 dB as compared to 900 MHz.

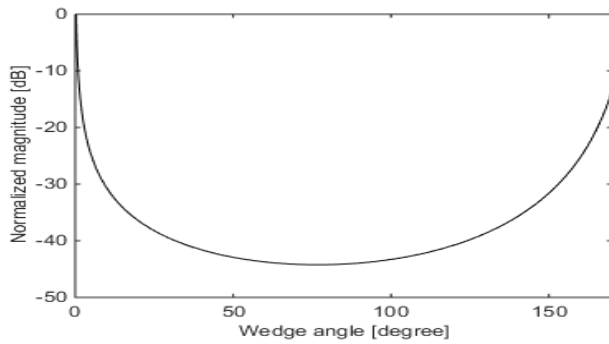
#### IV. THE TRACER ALGORITHM

As demonstrated earlier in Fig. 2, the channel can be considered to be LOS for small separation distance between  $T_X$ - $R_X$  in the range of 10 m. It is henceforth preferable to maximize the  $T_X$ - $R_X$  range as much as possible to capture the multipath phenomenon. Noting the limitation of the sounder,  $T_X$ - $R_X$  range (d) was set to 10 m. The free-space scattering can be decomposed into rays from objects surrounding both antennas as outlined below:

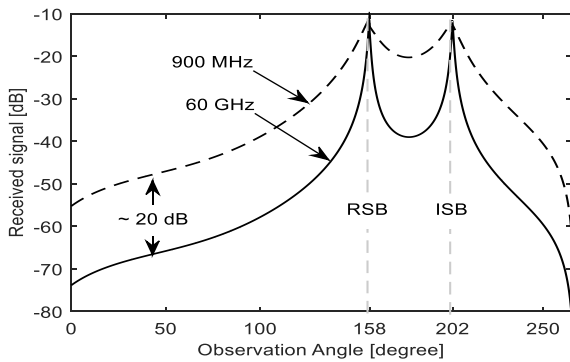




(a) Right wedge angle ( $f = 60$  GHz,  $\sigma = 0.258$  S/m,  $\epsilon_r = 11.56$ ,  $s' = 5.5$  m,  $s = 5.5$  m  $\varphi' = 67^\circ$ )



(b) Variable wedge angle ( $f = 60$  GHz,  $\sigma = 0.258$  S/m,  $\epsilon_r = 11.56$ ,  $s' = 5.5$  m,  $s = 5.5$  m  $\varphi' = 67^\circ$ )



(c) Right wedge angle ( $\sigma = 0.1$  S/m,  $\epsilon_r = 15$ ,  $s' = 28$  m,  $s = 27.5$  m  $\varphi' = 22^\circ$ )

FIGURE 4. UTD field computed using [20] and [21].

- *Free Space (LOS)*: For a direct LOS ray of path length ( $d$ ), the incident field at  $R_X$  is expressed as [26], [27]:

$$E_{LOS}(d) = G^T G^R \frac{E_o e^{-jk_\lambda d}}{d} \quad (13)$$

$G^T$  and  $G^R$  stand for  $T_X$  and  $R_X$  antenna gains, respectively. Their magnitudes are expressed in voltage units throughout the paper.  $\lambda$  is the wavelength and  $k_\lambda = 2\pi/\lambda$  represents

the wave number as a function of the wavelength.  $E_o$  is the relative amplitude of the spherical-wave source.

- *Reflection*: During measurements, the flat ground of the gallery was covered by a large mass of water which causes a specular reflection from the ground. In the 60 GHz band, the dielectric constant of pure water at  $20^\circ$  C is ( $\epsilon^* = 11.9 - j19.5$ ) as reported in [26]. Other reflected rays are generated by a flat rock in the ceiling located in the midway between  $T_X$  and  $R_X$ . Fresnel' reflection coefficients parallel and perpendicular polarizations are used to calculate reflected electric field pertained to these reflected rays:

$$E_R = E_o \sum_{i=1}^{n_r} G^T G^R R_i \frac{e^{-jkr^i}}{r^i} \quad (14)$$

" $n_r$ " denotes the number of the considered reflected rays from the surrounding surfaces that was set to two in this case.  $G^T$  and  $G^R$  are computed as functions of each angle of departure (AoD) and angle of arrival (AoA) of outgoing and incoming rays, respectively.  $R_i$  is the Fresnel reflection coefficient of the  $i^{th}$  reflected ray and " $r$ " is the distance travelled by the  $i^{th}$  reflected ray.

- *1<sup>st</sup>-order Diffractions ( $D_1$ )*: As described earlier, the surfaces of the mine constitute a group of diffracting wedges. Therefore, UTD diffraction phenomenon is likely to occur from the wedges of the ceiling, side-A and side-B as shown in Fig. 5. Depending on edges orientations, the tracer takes into account "soft case" diffractions from both, side-A and side-B and "hard case" diffractions from the ceiling of the gallery. Thus, the diffracted field can be expressed in terms of equations (3), (4) and (5) as:

$$E_{D_1}^{A,B,C} = E_o \sum_{i=1}^{n_A} \sum_{j=1}^{n_B} \sum_{k=1}^{n_C} G_{i,j,k}^T G_{i,j,k}^R D_{i,j,k} \times \frac{\sqrt{(s'_{i,j,k} + s_{i,j,k})}}{(s'_{i,j,k} + s_{i,j,k}) \sqrt{s'_{i,j,k} s_{i,j,k}}} \cdot \exp[-jk(s'_{i,j,k} + s_{i,j,k})] \quad (15)$$

$n_A$ ,  $n_B$ , and  $n_C$  are the number of wedges in surfaces A, B and ceiling (C), respectively.  $D_{i,j,k}$  are the diffraction coefficients associated with  $i^{th}$ ,  $j^{th}$  and  $k^{th}$  rays, respectively.  $s'_{i,j,k}$  and  $s_{i,j,k}$  are path lengths of incident and diffracted rays.

- *2<sup>nd</sup>-order Diffractions ( $D_2$ )*: Inclusion of doubly diffracted rays travelling from side-A to side-B (A→B) and (B→A) enhance the accuracy of calculations. Successive diffraction of rays by the wedges give rise to the enhancement of the power received at the Rx location by increasing the number of connecting in-phase rays as depicted in Fig. 5a. Second order diffraction rays are computed using Holm's approach [26] and the received field associated with (A→B)

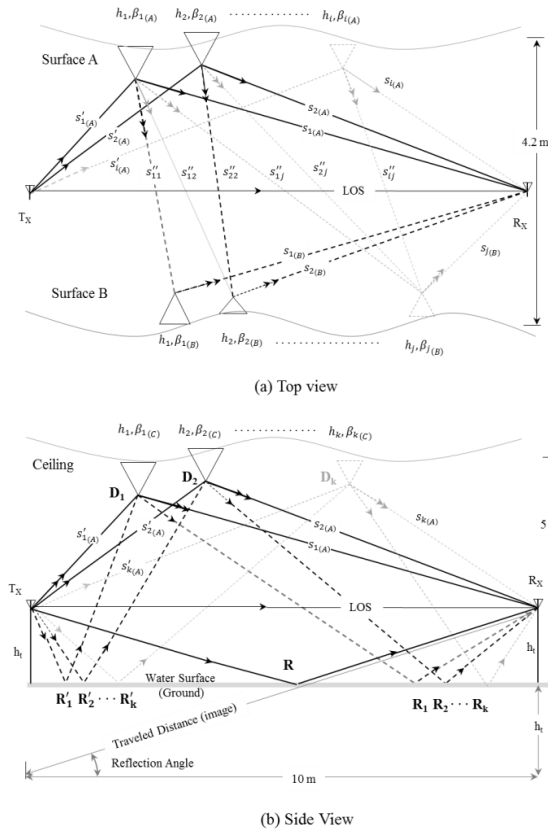


FIGURE 5. Propagation mechanisms in the undertaken gallery.

is expressed as follows:

$$E_{D_2}^{A \rightarrow B} = E_o \sum_{i=1}^{n_A} \sum_{j=1}^{n_B} G_i^T G_j^R D_i D_j \cdot \frac{\sqrt{(s'_i + s''_{ij} + s_j)}}{(s'_i + s''_{ij} + s_j) \sqrt{s'_i s''_{ij} s_j}} \cdot \exp \left[ -jk (s'_i + s''_{ij} + s_j) \right] \quad (16)$$

$D_i$  and  $D_j$  are the diffraction coefficients associated with  $i^{th}$  wedge of side-A and  $j^{th}$  wedge of side-B.  $s'_{ij}$  are the direct path lengths separating  $i^{th}$  wedge of A and  $j^{th}$  wedge of B.

First order diffracted rays from the ceiling (C) were calculated and compared to specular reflections from the ground (G) before or after diffraction using the following equation:

$$E_{D_1 R_1}^{C \rightarrow G} = \sum_{k=1}^{n_C} G_k^T G_k^R R'_k D_k \cdot \frac{\sqrt{(s'_k + s_k)}}{(s'_k + s_k) \sqrt{s'_k s_k}} \cdot \exp \left[ -jk (s'_k + s_k) \right] \quad (17)$$

As expected, the transmit wave decreases as it goes through multiple diffraction and reflection. On the other hand, inclusion of multiple scattering phenomena (i.e. reflection and diffraction) in the computer simulations enhances the accuracy of the algorithm. A given number of rays, namely, (A→C), (A→G), (B→C), (B→G), (C→G) and (G→C) rays were taken into account in the calculation to avoid exceeding

the available computational resources. The received power can be henceforth expressed as:

$$P_r(d) = \left| \sum_{i=1}^{n_f} E_{LOS} + E_R + E_{D_1}^{A,B,C} + E_{D_2}^{A \rightarrow B} + E_{D_2}^{B \rightarrow A} + E_{D_1 R_1}^{C \rightarrow G} + E_{D_1 R_1}^{G \rightarrow C} \right|^2 \quad (18)$$

## V. FREQUENCY ANALYSIS AND EXPERIMENTAL VALIDATION

### A. HOMOGENOUS CHANNEL RESPONSE

To further simplify the multipath representation, an ideal channel having homogenous surfaces is introduced and analyzed before proceeding into experimental validation of the tracer.

Therefore, the received signal is predicted on the basis of equal-dimensions marble wedges separated by a distance increment of 0.25 m. LOS and reflected rays and their normalized sum are identified in Fig. 6(a). A further addition of single-diffracted rays associated with side surfaces A and B yields the CTF of Fig. 6(b), while the relative amplitude of the received signal varies within 20 dB with large-scale fading trend that follows CTF of Fig. 6(a) and a small-scale fading that repeats every 57.2 MHz. It was found from the simulations that increasing the number of wedges does not cause a noticeable change in the fading rate. This is due to the small differential path lengths of 1<sup>st</sup>-order diffracted rays. Therefore, a minimum number of wedges can be considered in order to enhance the computational efficiency without compromising the accuracy. Similarly, adding 2<sup>nd</sup>-order diffractions to CTF of Fig. 6(b) leads to a selective frequency that occurs every 20 MHz as shown in Fig. 6(c).

The high fading rate stems from the inequality of the path lengths of the doubly-diffracted rays. Therefore, to keep the algorithm complexity tractable at ranges beyond 10 m, a limited number of wedges should be considered. Moreover, Fig. 6(d) shows the results of 1<sup>st</sup>-order diffracted rays from the ceiling (C) after their subjection to specular reflection mechanism from the ground. The fading occurs at a rate of about 31 MHz. Finally, the result shown in Fig. 6(e) included the effect of free-space LOS, reflected and up to the 2<sup>nd</sup>-order diffracted rays associated with the diverse surrounding surfaces.

### B. EXPERIMENTAL VALIDATION OF THE SIMULATED CTF

The randomness of underground mines results in a quite complicated propagation mechanism that renders the interpretation of the results rather complicated in the absence of the tracer that was presented in the previous sections of this paper [6].

Therefore, the tracer considers a group of wedges defined by random heights ( $h$ ) and angles ( $\beta$ ) with normal distributions between  $[-0.55 \text{ m}, +0.55 \text{ m}]$  with respect to their mean and within  $[1^\circ - 160^\circ]$ , respectively. Following Fig. 7, the random heights of the wedges cause an additional imbalance in the path lengths leading to higher variations in the differential phases among the propagated rays leading to significant

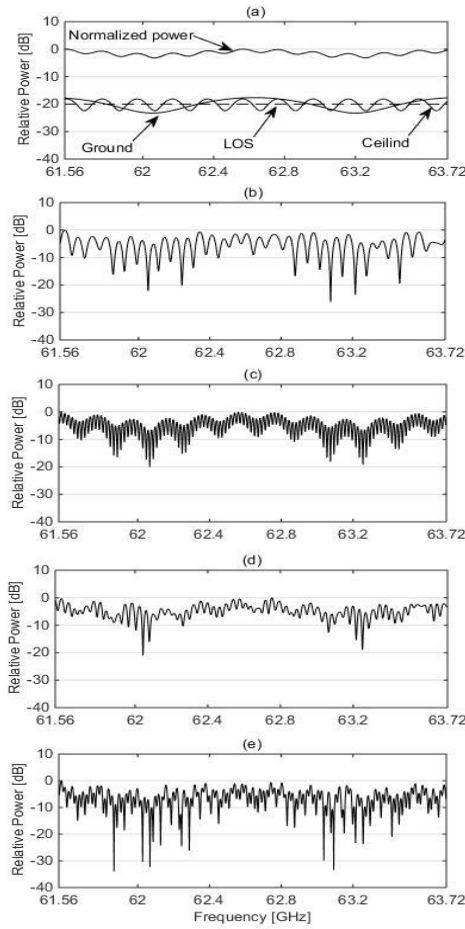


**FIGURE 6.** Analysis of CTF predicted at 10 m of  $T_x-R_x$  distance. (a) Ground and ceiling reflection effects. (b) 1<sup>st</sup>-order wedges diffractions from sides A, B and C. 2<sup>nd</sup>-order wedges diffractions i.e., (A→B) and (B→A). (d) 1<sup>st</sup>-order wedges diffracted rays from the ceiling subjected to reflections from the ground, i.e., (C→G) and (G→C). (e) Summation of all considered multipath.

fluctuation around a mean value. The effects of 1<sup>st</sup>-order diffractions on the received signal are shown in Fig. 7(a). The consideration of all contributions including 2<sup>nd</sup>-order diffractions results in the predicted CTF of Fig. 7(b). The number of wedges increase has a marginal impact and does not yield a noticeable change in the fading rate. Therefore, the number of wedges used in the calculations should comply with the available computational resources.

Figs. 7(a) and 7(b) demonstrate a good agreement between main features of calculated measured CTFs in terms of fading periodicity, scale and amplitude variation (within 35 dB). Numerous simulated sharp peaks, which are randomly distributed across the band of interest, were caused by severe variation in the dimensions of wedges as the incidence and diffraction angles approach of either ISB or RSB zones (c.f. Fig. 4). Furthermore, abrupt changes in the angles of the wedges can change the signal level by about 30 dB, as previously demonstrated in Fig. 4(b). Therefore, the presence of such wedges strengthens the multipath and causes the signal to fluctuates significantly around its mean value

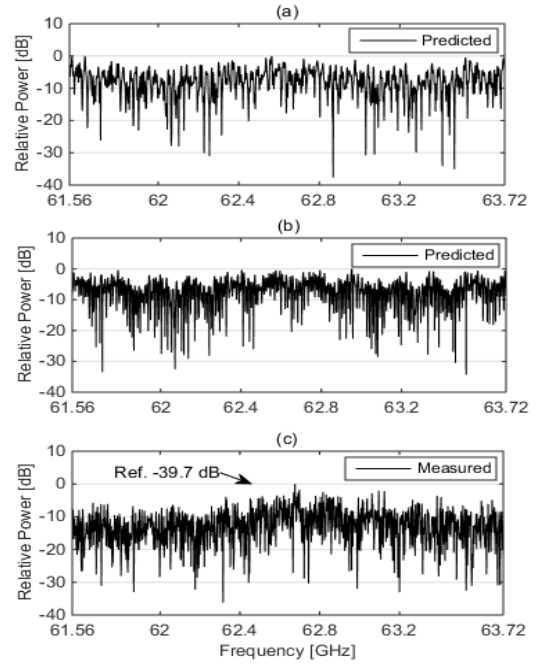


**FIGURE 7.** CTFs obtained at 10 m of  $T_x-R_x$  distance (a) Predicted using 1<sup>st</sup>-order wedges diffraction. (b) Predicted using 1<sup>st</sup>-order and 2<sup>nd</sup>-order wedges diffraction. (c) Measured CTF.

as the observation point moves in the gallery. This explains previously observed “location- specific” nature of propagation measurements in underground mine environments, which gives rise to the lognormal shadowing fading as reported in many studies [5], [6], [29]. However, in the absence of those extreme-sized wedge angles, the channel tends to behave as a Ricean channel.

## VI. TEMPORAL ANALYSIS AND EXPERIMENTAL VALIDATION

After the validation of the model in Frequency Domain (FD), further analysis was carried out in Time Domain (TD) to predict the dispersive characteristics of the channel and in order to validate the tracer. Indeed, the identification of each contributor in the measured Power Delay Profile (PDP) will be feasible with the use of the presented deterministic tool. The PDP is expressed as [21]:

$$PDP(t) = \sum_{i=0}^{n(t)} \alpha_i(t, \tau) \delta(t - \tau_i(t)) e^{j\theta_i(t, \tau)} \quad (19)$$

where “ $n$ ” is the number of multipath rays at a time “ $t$ ”,  $\alpha_i$ ,  $\tau_i$  and  $\theta_i$  are the magnitude, delay and phase  $i^{th}$  multipath ray and  $\delta(\cdot)$  denotes the Dirac delta function.

### A. SINGLE DIFFRACTION FROM HOMOGENOUS SURFACES

The analysis was simplified by isolating the contribution of each enclosing surface of an ideal homogenous channel. Subsequently, the effect of wedges on the PDPs was analyzed. Taking into account the polarization of the incident field,

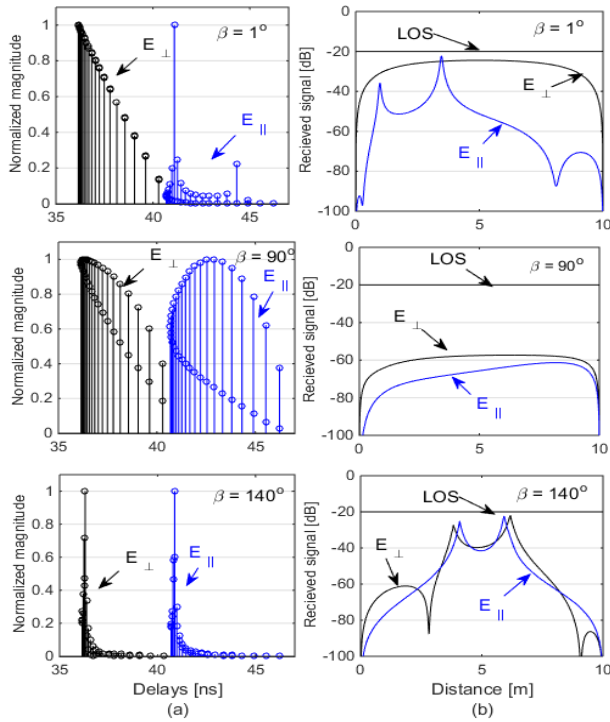


**FIGURE 8.** 1<sup>st</sup> order UTD from homogenous surfaces of the channel. a) Normalized PDP. b) UTD amplitude as a function of the wedge position.

PDPs were computed for the 1<sup>st</sup>-order diffractions from the homogenous surfaces of side A and ceiling. Fig. 8(a) shows three PDPs that were computed as a function of equal wedge angles of 1°, 90° and 140°.

The first ray was the result of the shortest path associated with the central wedge that followed by gradual smearing rays. Each pair of rays reached  $R_X$  at the same delay bin as a result of equal path lengths associated with the symmetrical locations of the wedges with respect to  $T_X$  and  $R_X$ . However, these pairs of rays were not necessarily equal in magnitudes because of different angles of incidence. The strength and variation of the PDP depend strongly on angles of the wedges, their locations and associated ISB/RSB angular positions. Fig.8(b) shows the simulated magnitude of diffraction as a function of the wedge position throughout side-A with respect to  $T_X$ . The soft ( $E_{\perp}$ ) diffraction from an almost knife edge (1°) was found to be important regardless of its position. The lower diffraction level in the vicinity of either  $R_X$  or  $T_X$  was due to the directional patterns of the antennas. On the other hand, the hard ( $E_{\parallel}$ ) diffraction from the ceiling is found to be insignificant except for the peaks associated with ISB and RSB angular positions of the wedge. The results computed for ( $\beta = 90^\circ$ ) confirmed the marginal impact of diffraction when angles of wedges are within (40°–120°) regardless of the polarization of the incident field. In contrast, for the case ( $\beta = 140^\circ$ ), the amplitude of the diffracted field was found to be considerably strong, especially when the wedge position reached either 4 m or 6 m that was associated with ISB and RSB angular regions of the wedge, respectively.

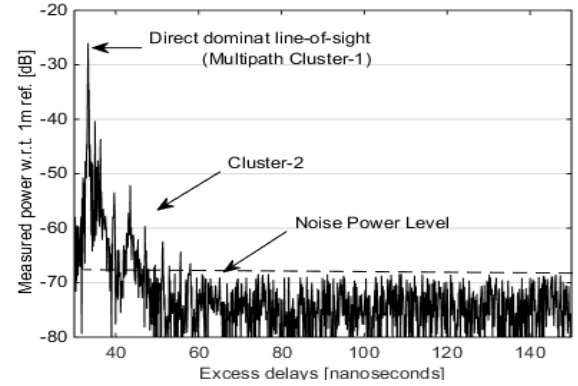


**FIGURE 9.** Channel's PDP measured at a Tx-Rx Range of 10 m.

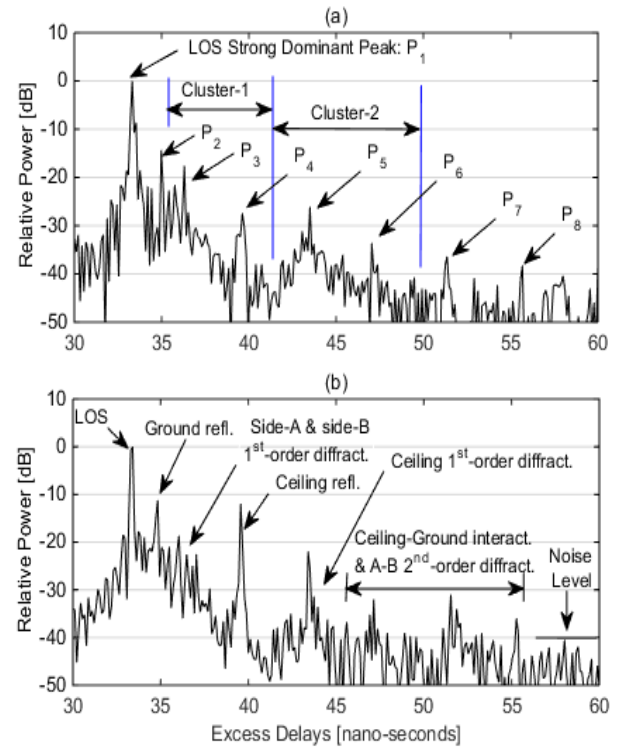


**FIGURE 10.** Normalized Channel's PDP Obtained at a Tx-Rx Range of 10m. a) Measurement and b) Prediction.

## B. TIME-DISPERSIVE VALIDATION OF THE TRACER

The channel's predicted and measured PDPs were computed by applying the Inverse Discrete Fourier Transform (IDFT) to CTFs of Fig. 7(b) and Fig. 7(c), respectively:

$$PDP_{dB} = 10 \log_{10} \left\{ |IDFT \{CTF\}|^2 \right\} \quad (20)$$

Fig. 9 shows the experimental PDP that shows two multipath clusters identified within a delay interval of (33ns–53ns) and the noise power level around –70 dB. The first perceptible ray was recorded at about –26 dB with an excess delay of 33.3 ns as a result of LOS free-space propagation. Further analysis has been performed with the aid of the tracer, in order to identify other multipath rays.



Normalized PDPs were zoomed out within (30ns-55ns) in Fig. 10 in order to capture their minute features. It can be observed that the experimental PDP is in good agreement with simulations in terms of multipath gain and delay.

The difference can be attributed to the hardware noise. In practice, the time resolution of the receiver might not be sufficient to resolve all multipath, i.e., there is still a high probability that more than one ray falls into a given resolvable delay bin and add up there. On the other hand, IDFT presents limitations due to the rounding to the nearest integer.

Having gone through the analysis that was outlined in the previous sections, it is feasible to offer a detailed description of the multipath propagation mechanisms and measurements for P2 to P8 peaks shown in Fig. 10(a):

P<sub>2</sub>: A specular reflection from the ground that was detected at about 34 ns and dominates the exponentially decreasing multipath cluster (Cluster-1).

P<sub>3</sub>: Was detected at 36.3 ns with a power magnitude of -18.7 dB. Analysis has shown that Cluster-1 is formed by a combination of two coinciding clusters resulted from 1<sup>st</sup>-order diffracted rays associated with side-A and side-B of the gallery. Cluster-1 that ends up at about 42 ns is interfered by a specularly reflected ray from the ceiling (P<sub>4</sub>).

P<sub>5</sub>: Its delay was 43 ns with -26 dB peak that dominated cluster-2, which was the result of 1<sup>st</sup>-order diffractions from the ceiling of the mine. The non-monotonic decaying behavior of Cluster-2 is due to the interference of 2<sup>nd</sup>-order diffracted rays (including P<sub>6</sub>) from side-A to side-B and vice versa.

Finally, P<sub>7</sub> and P<sub>8</sub> were detected at 51.36ns and 55.7ns, respectively, and their main physical propagation was the interaction between the ceiling and the ground as demonstrated earlier.

## VII. DISCUSSION AND CONCLUSION

This work presents an RT simulator to predict characteristics of mm-wave propagation in underground mine tunnels. Unlike indoor environments, specular reflections from surrounding rough surfaces of randomly-structured tunnels impact the propagation significantly. Consequently, the diffraction phenomenon was evident since the rough surfaces appear as groups of diffracting wedges to the propagating signal at short wavelengths. Therefore, each surface of the gallery was modeled as a group of wedges having random dimensions (heights, angles) being transversely oriented throughout the gallery.

In the presented model, Remley's UTD expression was found to be the right option for achieving relevant results as it accounted for the dielectric constant of diffracting edges and provided good approximation when the receiver was in the deep shadow region. Furthermore, the tracer has revealed the "location-specific" nature of collected data for underground mines which were reported in the previous literature. In fact, the domination of wedges with angles in the vicinities of 1° and 140° intensified the multipath and caused the signal to fluctuate significantly around LOS component from one

location to another throughout the gallery. This gave rise to the lognormal shadowing fading phenomenon. In contrast, the absence of those wedges weakened the multipath and gave rise to a LOS Ricean channel.

## REFERENCES

- [1] C. Briso-Rodriguez, P. Fratilesco, and Y. Xu, "Path loss modeling for train-to-train communications in subway tunnels at 900/2400 MHz," *IEEE Antennas Wireless Propag. Lett.*, vol. 18, no. 6, pp. 1164–1168, 2019.
- [2] C. Zhou and R. Jacksha, "Modeling and measurement of radio propagation in tunnel environments," *IEEE Antennas Wireless Propag. Lett.*, vol. 16, pp. 1431–1434, 2017.
- [3] L. Zhou, F. Luan, S. Zhou, A. Molisch, and F. Tufvesson, "Geometry-based stochastic channel model for high-speed railway communications," *IEEE Trans. Veh. Technol.*, vol. 68, no. 5, pp. 4353–4366, Mar. 2019.
- [4] H. Kunsei, K. S. Bialkowski, M. S. Alam, and A. M. Abbosh, "Improved communications in underground mines using reconfigurable antennas," *IEEE Trans. Antennas Propag.*, vol. 66, no. 12, pp. 7505–7510, Sep. 2018.
- [5] M. Ghaddar, L. Talbi, I. Ben Mabrouk, and M. Nedil, "Multiple-input multiple-output beam-space for high-speed wireless communication in underground mine," *IET Microw., Antennas Propag.*, vol. 10, no. 1, pp. 8–15, 2016.
- [6] M. Ghaddar, L. Talbi, M. Nedil, I. B. Mabrouk, and T. A. Denidni, "Mm-waves propagation measurements in underground mine using directional MIMO antennas," *IET Microw., Antennas Propag.*, vol. 10, no. 5, pp. 517–524, Apr. 2016.
- [7] S. F. Mahmoud and J. R. Wait, "Geometrical optical approach for electromagnetic wave propagation in rectangular mine tunnels," *Radio Sci.*, vol. 9, no. 12, pp. 1147–1158, Dec. 1974.
- [8] A. Emslie, R. Lagace, and P. Strong, "Theory of the propagation of UHF radio waves in coal mine tunnels," *IEEE Trans. Antennas Propag.*, vol. AP-23, no. 2, pp. 192–205, Mar. 1975.
- [9] R. Martelly and R. Janaswamy, "An ADI-PE approach for modeling radio transmission loss in tunnels," *IEEE Trans. Antennas Propag.*, vol. 57, no. 6, pp. 1759–1770, Jun. 2009.
- [10] K. Guan, B. Ai, B. Peng, D. He, G. Li, J. Yang, Z. Zhong, and T. Kürner, "Towards realistic high-speed train channels at 5G millimeter-wave band—Part I: Paradigm, significance analysis, and scenario reconstruction," *IEEE Trans. Veh. Technol.*, vol. 67, no. 10, pp. 9112–9128, Aug. 2018.
- [11] I. Ben Mabrouk, J. Hautcoeur, L. Talbi, M. Nedil, and K. Hettak, "Feasibility of a millimeter-wave MIMO system for short-range wireless communications in an underground gold mine," *IEEE Trans. Antennas Propag.*, vol. 61, no. 8, pp. 4296–4305, Aug. 2013.
- [12] M. E. Khaled, P. Fortier, and M. L. Ammari, "A performance study of line-of-sight millimeter-wave underground mine channel," *IEEE Antennas Wireless Propag. Lett.*, vol. 13, pp. 1148–1151, 2014.
- [13] Z. He, T. Su, H.-C. Yin, and R.-S. Chen, "Wave propagation modeling of tunnels in complex meteorological environments with parabolic equation," *IEEE Trans. Antennas Propag.*, vol. 66, no. 12, pp. 6629–6634, 2018.
- [14] Y. Jiang, G. Zheng, X. Yin, A. Saleem, and B. Ai, "Performance study of millimeter-wave MIMO channel in subway tunnel using directional antennas," *IET Microw., Antennas Propag.*, vol. 12, no. 5, pp. 833–839, 2018.
- [15] I. B. Mabrouk, L. Talbi, and M. Nedil, "Performance evaluation of a MIMO system in underground mine gallery," *IEEE Antennas Wireless Propag. Lett.*, vol. 11, pp. 830–833, 2012.
- [16] X. Yin, G. Zheng, and A. Saleem, "Influence of antenna configuration on mm-wave MIMO performance in a subway-like tunnel," *IET Microw., Antennas Propag.*, vol. 12, no. 15, pp. 2395–2401, 2018.
- [17] M. Ghaddar, L. Talbi, G. Y. Delisle, and J. LeBel, "Deflecting-obstacle effects on signal propagation in the 60 GHz band," *IEEE Trans. Antennas Propag.*, vol. 61, no. 1, pp. 403–414, Jan. 2013.
- [18] M. Jacob, S. Priebe, R. Dickhoff, T. Kleine-Ostmann, T. Schrader, and T. Kürner, "Diffraction in mm and sub-mm wave indoor propagation channels," *IEEE Trans. Microw. Theory Techn.*, vol. 60, no. 3, pp. 833–844, Mar. 2012.
- [19] V. Degli-Esposti, F. Fuschini, E. M. Vitucci, M. Barbiroli, M. Zoli, L. Tian, X. Yin, D. A. Dupleich, R. Müller, C. Schneider, and R. S. Thomä, "Ray-tracing-based mm-wave beamforming assessment," *IEEE Access*, vol. 2, pp. 1314–1325, 2014.

- [20] M.-T. Martínez-Inglés, D. P. Gaillot, J. Pascual-García, J.-M. Molina-García-Pardo, M. Lienard, and J.-V. Rodríguez, "Deterministic and experimental indoor mmW channel modeling," *IEEE Antennas Wireless Propag. Lett.*, vol. 13, pp. 1047–1050, May 2014.
- [21] T. S. Rappaport, *Wireless Communications: Principles and Practice*, 2nd ed. Upper Saddle River, NJ, USA: Prentice-Hall, 2001.
- [22] D. A. McNamara, C. W. I. Pistorius, and J. A. G. Malherbe, *Introduction to the Uniform Geometrical Theory of Diffraction*. Norwood, MA, USA: Artech House, 1990.
- [23] R. J. Luebbers, "Finite conductivity uniform UTD versus knife diffraction prediction of propagation path loss," *IEEE Trans. Antennas Propag.*, vol. AP-32, no. 1, pp. 70–76, Jan. 1984.
- [24] L. Correia and P. Frances, "Estimation of materials characteristics from power measurements at 60 GHz," in *Proc. 5th IEEE Int. Symp. Pers., Indoor Mobile Radio Commun.*, The Hague, The Netherlands, Sep. 1994, pp. 510–513.
- [25] K. A. Remley, H. R. Anderson, and A. Weissar, "Improving the accuracy of ray-tracing techniques for indoor propagation modeling," *IEEE Trans. Veh. Technol.*, vol. 49, no. 6, pp. 2350–2358, Nov. 2000.
- [26] P. D. Holm, "A new heuristic UTD diffraction coefficient for nonperfectly conducting wedges," *IEEE Trans. Antennas Propag.*, vol. 48, no. 8, pp. 1211–1219, Aug. 2000.
- [27] D. M. Pozar, *Microwave and RF Design of Wireless Systems*, 2nd ed. Hoboken, NJ, USA: Wiley, 2000.
- [28] S. Gezici, I. Guvenc, Z. Sahinoglu, and U. C. Kozat, Eds., *Reliable Communications for Short-Range Wireless Systems*. Cambridge, U.K.: Cambridge Univ. Press, 2011.
- [29] M. Boutin, A. Benzakour, C. L. Despins, and E. Affés, "Radio wave characterization and modeling in underground mine tunnels," *IEEE Trans. Antennas Propag.*, vol. 4, no. 5, pp. 540–549, Feb. 2008.



**MOHAMAD GHADDAR** was born in Beirut, Lebanon. He received the M.Sc. degree in wireless telecommunications from the International Institute of Telecommunications, Montréal, Canada, in 2004, and the Ph.D. degree in electrical engineering and information technology (radio frequency) from the University of Quebec, Canada, in 2012.

He was a Research Scientist with the Wireless Propagation Division, Communication Research Center, Ottawa, Canada, from 2008 to 2012, and a Postdoctoral Research Associate with the University of Quebec, from 2013 to 2017. He is currently a Research Associate with the LRTCS Wireless Lab, Canada. His general research interests focus on 5G wireless networks measurement, simulation, and modeling, and digital signal processing. His research interests include the design and development of wireless network optimization simulators for MIMO and OFDM systems, and link budget optimization and capacity estimation for terrestrial wireless systems. He has been involved in editorial activities for Technical and Signal Processing Journals.



**ISMAIL BEN MABROUK** received the B.A.Sc. and M.A.Sc. degrees in electrical engineering from the University of Lille, Lille, France, in 2006 and 2007, respectively, and the Ph.D. degree in electrical engineering from the University of Quebec, Canada, in 2012. From 2007 to 2009, he was with Huawei Technologies, Paris, France. In 2012, he joined the Wireless Devices and Systems (WiDeS) Group, University of Southern California, Los Angeles, CA, USA. He is currently an

Assistant Professor with the Al Ain University of Science and Technology, Abu Dhabi, UAE. His research activities have been centered on propagation studies for multiple-input and multiple-output (MIMO) systems, measurement campaigns in special environments, WBAN, and antenna design at the millimeter-wave and THz frequencies.



2008. In June 2008, he joined the Engineering School Department, University of Quebec at Abitibi-Témiscamingue, Quebec, Canada, where he is currently a Full Professor. His research interests include antennas, MIMO radio-wave propagation, and microwave devices.



**KHELIFA HETAK** received the Dipl.Ing. degree in telecommunications from the University of Algiers, Algeria, in 1990, and the M.A.Sc. and Ph.D. degrees in signal processing and telecommunications from University of Rennes 1, France, in 1992 and 1996, respectively.

In January 1997, he has been with the Personal Communications Staff of INRS-Télécommunications, where he was involved. He joined the Electrical Engineering Department, Laval University, since October 1998, as an Associate Researcher, where he was involved in RF aspects of smart antennas. Since August 1999, he has been with Terrestrial Wireless Systems Branch, Communications Research Centre (CRC), Ottawa, Canada, as a Research Scientist. He was involved in developing MMICs at 60 GHz, low temperature cofired ceramic (LTCC) packaging, RF MEMS switches, and GaN robust Tx/Rx modules. He is actively involved in microwave/millimeter-wave systems and related front-end analog electronic circuits, phased arrays, and satellite communication systems. He also is active in planar antenna design including wide scan-angle antennas at 60 GHz for wireless applications. He recently started an effort in CMOS/SiGe RFIC design for the 60 GHz region, with the particular emphasis on developing miniature phase shifters using CMOS/SiGe technology for phased-array applications, oscillators, and switches for millimeter-wave communication systems.



**LARBI TALBI** (S'95–M'97–SM'05) received the Ph.D. degree in electrical engineering from Laval University, Quebec, in 1994. He is currently a Full Professor with the Department of Computer Science and Engineering, University of Quebec in Outaouais (UQO), Gatineau. He completed a Postdoctoral Fellowship with the Personal Communications Research Group, INRS-Télécommunications, Montreal, QC, Canada (1994–1995), where he led a project supported by

Bell-Canada. In 2005, he spent his sabbatical leave with the Communication Research Center (CRC), Ottawa, with the Propagation Research (RVEP) Group, Satellite Communications and Radio Propagation Branch (VPSAT). In 2006, he was a Visiting Professor with the Electrical and Electronics Engineering Department, Dumlupinar University, Turkey. Beside CRC, he has also a very strong collaboration with the Telebec Wireless Underground Communication Laboratory, Val-d'Or, Quebec. He has authored and coauthored over 250 journal and conference technical papers. His research activities include experimental characterization and modeling of indoor radio propagation channels for 5G applications, and design of microwave circuits and antennas using SIW and FSS techniques. Currently, he is actively involved in a major project related to the deployment of wireless technologies in underground mines using MIMO technique. He has many industrial collaborations. In 2017, he obtained a patent with Nokia for the design of dual-band power amplifier using metamaterials. He is a member of the Order of Engineers of Quebec. In 2013, he was awarded the Best Paper Prize of IET - ICWCA Conference held in Malaysia.

...